Journal of Materials Chemistry A

ROYAL SOCIETY OF CHEMISTRY

PAPER

Published on 28 August 2026

Cite this: DOI: 10.1039/d6ta05248g

Tailoring thermal mass for enhanced infrared response in Sb–Bi–Te-based printed thermocouples

Amrutha Bose,[a] Zirui Wang,[b] Muhammad Irfan Khan,[b] Leonard Franke,[be] Apoorv Kulkarni,[b] Stefan Heißler,[c] Heidemarie Schmidt,[d] Mohamed Hussein,[bf] Uli Lemmer*[ab] and Md Mofasser Mallick*[be]

Received 22nd June 2026
Accepted 28th August 2026

DOI: 10.1039/d6ta05248g

rsc.li/materials-a

Recent developments in the fabrication of advanced materials have broadened the application space of thermoelectric (TE) technologies beyond conventional solid-state cooling and energy harvesting. A compelling application is the use of TE materials to facilitate photo-thermoelectric (PTE) infrared sensing *via* a dual-stage energy conversion process: radiation-to-thermal followed by thermal-to-electric. Here, we report a detailed study on dimensionally controlled, screen-printed PTE infrared sensors fabricated on flexible substrates. We tune the thickness of Bi–Sb–Te-based p- and n-type printed TE films *via* ink formulation to study the thermal mass dependent optical, microstructural, mechanical and thermoelectric properties, and their combined effect on PTE sensing performance. Single-legged and double-legged printed PTE sensors were fabricated using p- and n-type Bi–Sb–Te materials. Under CO_2 laser irradiation with 10.6 μm wavelength, the double-legged PTE sensor showed a peak responsivity of 107.7 mV W^{-1}. Finite-element simulations were also performed to validate the experimental findings. These results highlight thermal mass engineering as an effective pathway toward high-performance, flexible, non-contact human–machine interaction systems and proximity sensors.

1. Introduction

Thermoelectric (TE) technology has been a key area of research across a wide range of applications, from waste heat recovery and energy harvesting to localized cooling.[1,2] The solid-state operation of this technology, without the need for external bias or working fluids, along with a long lifetime and minimal maintenance, makes it particularly attractive.[3] However, an important yet comparatively overlooked research area beyond energy conversion is thermal sensing based on the TE effect. Recent progress in advanced TE material synthesis and processing has led to increased adoption of this technology for thermal sensing applications, including temperature and infrared (IR) sensing.[4–6] For thermal sensing, sensor thermocouples absorb incident radiation, causing localized heating of one junction and creating a spatial temperature gradient *via* a photo-thermal conversion process (*cf.* Fig. 1(a)). This temperature gradient is then transformed into a readable electric voltage 'V_{out}' *via* the Seebeck effect:

$$V_{out} = N\alpha(T_h - T_c) \quad (1)$$

where 'N' is the number of thermocouples, $\alpha = \alpha_p + \alpha_n$ is the total Seebeck coefficient, and T_h and T_c are the hot and cold side temperatures of the thermocouple, respectively. IR sensors based on the photo-thermoelectric effect (PTE) are promising for proximity sensing, thermal imaging, and environmental monitoring applications due to their advantages over semiconductor photodetectors which do not require cooling to low temperatures. Furthermore, unlike semiconductor IR sensors, a PTE sensor enables broadband spectral response from the near- to long-wavelength (3–15 μm) infrared regions without bandgap constraints.[7–10] Also, PTE infrared sensors consume less power, exhibit high stability, and require no external bias. The sensor performance is influenced by optical absorption, thermal mass, and geometry, as these parameters govern photothermal conversion efficiency and sensor responsivity.[11] Carbon-based composites, such as carbon nanotubes (CNTs) embedded in poly(3,4-ethylenedioxythiophene): poly(styrenesulfonate) (PEDOT: PSS), have shown the ability to operate flexibly and are self-powered for PTE sensing when exposed to blackbody radiation. They also exhibit stable bending performance. A graphene–

[a]Institute of Microstructure Technology, Karlsruhe Institute of Technology (KIT), 76344 Eggenstein-Leoppoldshafen, Germany. E-mail: uli.lemmer@kit.edu

[b]Light Technology Institute, Karlsruhe Institute of Technology (KIT), 76131 Karlsruhe, Germany. E-mail: mofasser.mallick@kit.edu

[c]Institute of Functional Interfaces, Karlsruhe Institute of Technology (KIT), 76344 Eggenstein-Leopoldshafen, Germany

[d]Abbe School of Photonics, Friedrich Schiller University Jena, 07745 Jena, Germany

[e]varmo GmbH, 76433 Eggenstein-Leopoldshafen, Germany

[f]Ain Shams University, Department of Physics, Faculty of Science, Abbassia, Cairo, Egypt

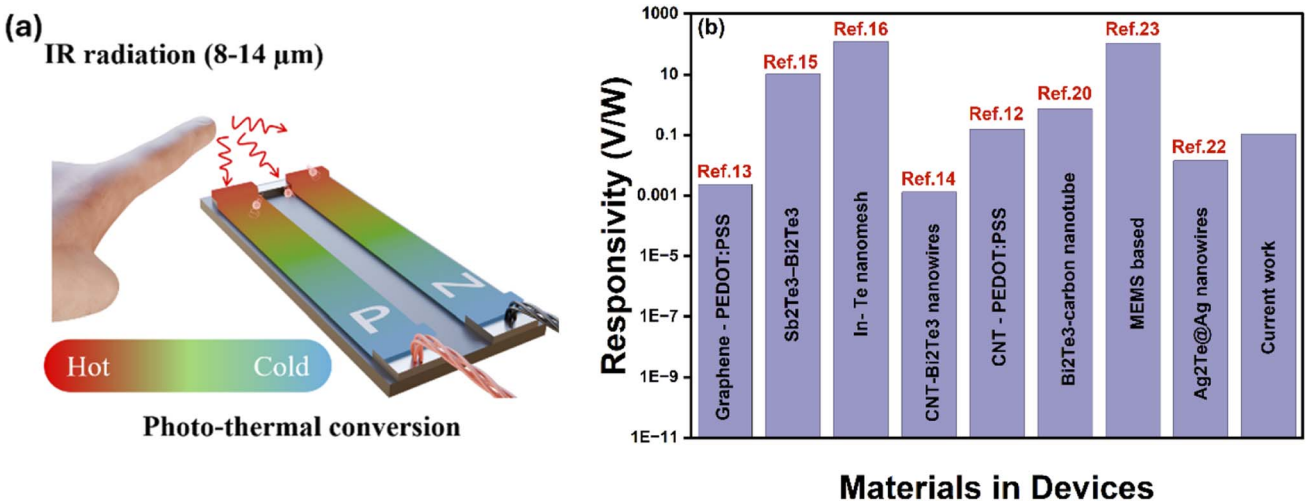

Fig. 1 (a) Schematic representation of the photo-thermoelectric effect and (b) comparison of responsivities in reported literature studies with the present work. The literature values are from different material systems, device geometries and experimental conditions and are intended to provide a general comparison of reported performance.

PEDOT: PSS composite-based PTE sensor exhibited a responsivity of 0.00227 V W^{-1}.[12,13] Through synergistic interactions between nanowires, hybrid CNT–Bi_2Te_3 PTE devices exhibited a responsivity of 0.00128 V W^{-1}.[14] Tellurium-based systems have been reported to exhibit strong PTE responses. For example, a Sb_2Te_3–Bi_2Te_3 PTE sensor showed a responsivity of 10.2 V W^{-1} at a bandwidth of 1 kHz, and Te nanomesh and multilayer structures exhibited a responsivity of up to 120 V W^{-1} with fast response times of about 17 ms and broad thermal sensing.[15,16] A flexible Te/Ag heterojunction film with a high Seebeck coefficient of 355 μV K^{-1} is reported to have a stable photothermal output. Bi_2Te_3 thin films and nanostructures with resonant nanophotonic designs enable LWIR-FIR detection over a wide range of wavelengths (8–20 μm) with a responsivity of 3.88 × 10^{-4} A W^{-1}.[17–19] Emerging materials like MXene-based flexible PTE detectors, Ag_2Te nanowire composites with high thermal responsivity and Bi_2Te_3 nanocrystal/single wall CNT networks with 0.71 V W^{-1} responsivity further enrich the landscape even more.[20–24] Notably, Bi_2O_2Se/InSe heterojunction photodetectors achieved a responsivity of 0.47 A W^{-1} under broadband and self-powered operation. This collectively highlights the significant progress and potential of advanced TE materials in PTE infrared sensing technology.[25] Even though self-powered PTE sensors have come a long way, they still lack mechanical robustness, shape-conformability and scalability. Printing methods, including screen printing,[6,26] can facilitate customization and scalability.

Fig. 1(b) compares the responsivities in reported literature studies and the present work. However, due to lack of detailed device structures including number of thermocouples, their normalized responsivities were not possible to estimate. Although several high-performance photo-thermoelectric IR sensors have been reported, which use advanced nanostructured materials and a higher number of thermocouples, their fabrication often involves complex processing routes and limited scalability. Bi–Sb–Te based-TE materials are promising for PTE sensing applications due their high Seebeck coefficients and high radiation absorptance. However, conventional fabrication techniques for these compounds including melt-spinning, spark plasma sintering and cold sintering, are complex and require multiple processing steps.[26,27] However, screen-printing is a low-cost and scalable technique that allows the fabrication of TE devices on both rigid and flexible substrates with high shape versatility. These factors make screen printing a promising manufacturing technique for the development of flexible and scalable IR sensors.

This work reports fully printed PTE infrared sensors based on Bi–Sb–Te TE films. A comprehensive analysis of how thickness control influences optical absorption, microstructure, mechanical flexibility, and PTE infrared sensing properties of the sensors was carried out. We have investigated the interaction of infrared radiation with 10.6 μm wavelength (corresponding to the maximum of blackbody radiation for $T = 300$ K) with both n-type ($Bi_2Te_{2.7}Se_{0.3}$) and p-type ($Bi_{0.5}Sb_{1.5}Te_3$) printed TE films on a flexible substrate. We have demonstrated that film-thickness optimization enhances absorbance and responsivity while maintaining mechanical robustness, achieving a responsivity of 107.7 mV W^{-1} for a double-legged printed PTE infrared sensor. Additionally, finite-element simulations were carried out and detail the thermal-electrical behavior and support device design. Our results underscore the potential of printed PTE infrared sensors for different applications, including flexible non-contact human–machine interaction systems, proximity sensors and wearable electronics. Rather than introducing a new material system, this work establishes thermal-mass engineering as an effective design strategy for printed IR sensors.

2. Experimental methods

2.1. Materials

TE bulk ingots (p-type $Bi_{0.5}Sb_{1.5}Te_3$ and n- type $Bi_2Te_{2.7}Se_{0.3}$) (EVERREDtronics), copper powder (spheroidal) (10–25 μm, 98%, Sigma-Aldrich), selenium powder (100 mesh, ≥99.5%

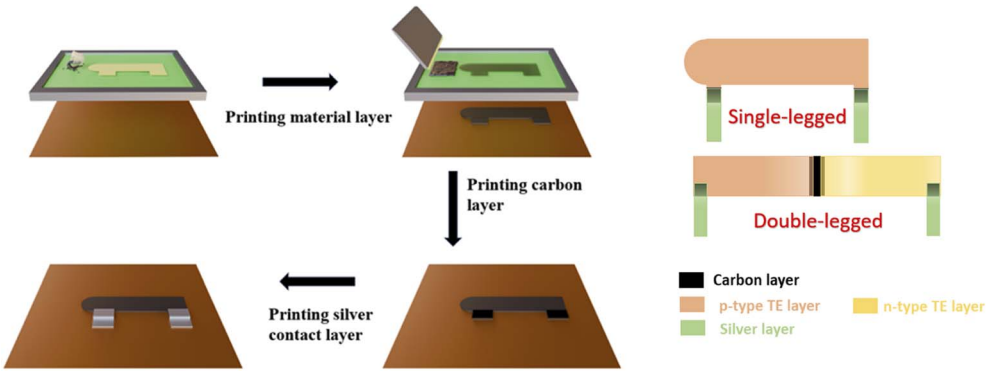

Fig. 2 Schematic representation of the fabrication process of the PTE infrared sensors.

trace metals basis, Sigma-Aldrich), *N*,*N*-diethyl formamide (DEF) (Sigma-Aldrich), terpineol (Sigma-Aldrich), polyvinylpyrrolidone (PVP) (average $M_w \sim 40\,000$, Sigma-Aldrich) and a Kapton substrate (50 μm DuPont de Nemours).

2.2. Preparation of TE inks

The preparation of Bi–Sb–Te-based n- and p-type inks involved a carefully controlled process to ensure the desired composition and consistency for printing applications.[28] Initially, the total ink weight was determined, and the amounts of solute and solution were calculated based on the target solid-to-solution ratio, which can range from 65% to 80% solids and 20% to 35% solution by weight. TE bulk ingots (p-type $Bi_{0.5}Sb_{1.5}Te_3$ and n-type $Bi_2Te_{2.7}Se_{0.3}$) were ground using a coffee grinder. The binder that contains elemental copper powder and selenium powder in a 2 : 1 ratio at 5 wt% for p-type and 10 wt% for n-type was weighed and added along with the active ingredient. The solution comprised 92% solution (by weight), with DEF accounting for 30–40% and TEP for 60–70%. The remaining 8% of the solution was the binder PVP, which provides adhesion and stability. After determining the appropriate solvent weight, PVP was combined with DEF and mixed using a magnetic stirrer at 1000 rpm for 10 min to form a homogeneous mixture. TEP was then added to the mixture and stirred once more. Using a planetary ball-milling jar (Fritsch Planetary Mill PULVERISETTE 5 premium-line), the active material, binder, and prepared solution were added and thoroughly mixed with a spatula. Then, the jars were sealed, and for approximately five minutes, a continuous, mild stream of nitrogen gas was flushed through them. We used 10 mm ZrO_2 balls (3 g) for 60 minutes at 350 rpm in a 120 ml jar, with a ball-to-powder ratio of 4 : 1. This process produced inks with the desired consistency and properties, ready for printing, in three variations prepared with solid-to-solution ratios of 80 : 20, 75 : 25, and 65 : 35, respectively. The rheology of the prepared ink with 20 percentage and 35 percentage solution was measured, tabulated (*cf.* Tables S5 and S6) and compared.

2.3. Fabrication of printed PTE infrared sensors

The screen-printing technique was employed to fabricate PTE infrared sensors using a semi-automated RokuPrint machine. A gap of approximately 2 mm was maintained between the screen and the substrate during printing. Printing was performed on a 50 μm-thick Kapton substrate, starting with the deposition of the p- and n-type TE materials (*cf.* Fig. 2). After drying the deposited TE inks, carbon and silver inks were printed to form the contacts. The drying temperature for both inks was maintained at 363 K. After proper drying, the fabricated device was sintered at 623 K for 10 min in an inert environment.

The device's resistance decreased, along with improved performance and stability, while the device's mechanical flexibility was maintained. Single-legged and double-legged PTE infrared sensors with three different thicknesses, $t_1 = 12 \pm 1$ μm, $t_2 = 23 \pm 1$ μm, and $t_3 = 30 \pm 1$ μm, were fabricated. Theoretical thickness was calculated from the screen parameters and the ink volume equation. The ink transfer efficiency is also studied (*cf.* Table S5).

2.4. The characterization techniques of printed TE films and PTE sensors

To understand the structural, morphological, and functional properties of the printed TE materials, several characterization techniques were employed. The infrared absorption was examined using diffuse reflectance infrared Fourier transform spectroscopy (DRIFTS) with a Bruker Vertex 80 FTIR spectrometer equipped with a Spectra Tech DRIFTS accessory. A JEOL JCM-5700 scanning electron microscope (SEM) provided accurate information on surface morphology. The Seebeck coefficient (α) and electrical conductivity (σ) were measured using a Linseis HCS 10 to evaluate the thermoelectric performance. The optoelectronic response to 10.6 μm laser irradiation using a Coherent Diamond C-20 CO_2 laser was investigated to assess photothermal conversion behavior.

3. Results and discussion

The PTE infrared sensors were printed using three TE inks with varying rheologies, resulting in varying thicknesses. The measured sensor thicknesses were $t_1 = 12 \pm 1$ μm, $t_2 = 23 \pm 1$ μm, and $t_3 = 30 \pm 1$ μm for solvent contents in the inks of 35 wt%, 25 wt%, and 20 wt%, respectively. In the following section, the sample with a thickness of t_1 and p-type character is

denoted as sample #1, p. The other samples are denoted accordingly with "d" indicating the double-legged devices.

3.1. Optical and microstructural properties of printed p- and n-type TE films

The optical properties of p- and n-type printed TE films in the IR spectral range were characterized by diffuse reflectance infrared Fourier transform spectroscopy (DRIFTS) as shown in Fig. 3. The optical parameters, the absorptance, reflectance, and transmittance of the printed TE films are essential for the underlying PTE performance. To understand the impact of film thickness on optical properties, the p- and n-type printed films with three different thicknesses (t_1, t_2, and t_3) were analyzed. In general, all three samples exhibited high absorptance (above 65%) at 10.6 μm, indicating that the PTE effect is suitable for human-body detection. Specifically, the intermediate thickness t_2 of both p- and n-type printed TE films showed the highest absorptances at 77% and 67%, respectively, compared to the nominally thickest and thinnest films. This can be attributed to the factors revealed by the reflection and transmission spectra, and the microscopic images. The optical properties not only rely on the nominal film thickness but also on morphology. At a wavelength of 10.6 μm, sample # 2, n and sample # 2, p exhibited the lowest reflectance and highest absorptance.

The high solute concentration enables thicker films; however, the films dry faster and form larger particles and more voids after drying and sintering, as shown in Fig. 4(a) and (d). These particles will scatter more radiation, increasing diffuse reflectance. In the meantime, the porosity of the thickest film allowed photons to pass through the voids, thereby increasing the measured transmittance. Both high reflectance and transmittance result in relatively low absorptance, as shown in Fig. 3(b) and (e). The lower solute concentration in the ink results in smaller particles and thinner films. In brief, these printed Sb–Bi–Te films exhibited strong absorptance and low transmittance, suggesting the possibility of effective localized heating without an external absorber in a PTE device. More importantly, rheological modification tunes the thickness of the printed films to achieve higher optical absorption, thereby improving device performance. The SEM micrographs (see Fig. 4) of printed p- and n-type TE films clearly show irregular plate-like particles with sharp edges. The microstructure shows the effect of solution percentage on mechanical grinding during ink processing. As the solvent content increases, the thickness decreases, and the surface becomes more densely packed, with a smaller particle size. The thicker films show larger, more distinct grains and exhibit more voids and irregularities, indicating less uniform surface roughness. As the sample thickness decreases, the microstructure becomes more compact and finer. Thinner samples also show a smoother, more uniform surface with fewer visible voids. So, a reduction in thickness leads to more compact films and reduced porosity, which can improve mechanical strength and other functional properties, such as absorptivity. The SEM images were analyzed in more detail to quantify the area fraction of voids. The results are summarized in Table S2, and it clearly shows that there is an evident change in the percentage of the area fraction of voids with thickness change. This indicates a strong microstructural evolution that has an influence on the optical characteristics. But optical absorption also depends on multiple factors and so the void fraction alone cannot fully explain the optical properties.

3.2. Mechanical properties of printed p- and n-type TE films

To evaluate the sensor's durability under mechanical stress, a stability study is essential. Hence, bending and unbending tests of the printed TE films around two rods with diameters (D) of 4.49 mm and 2.49 mm, respectively, were performed for 100 cycles. The resistance was measured several times during the

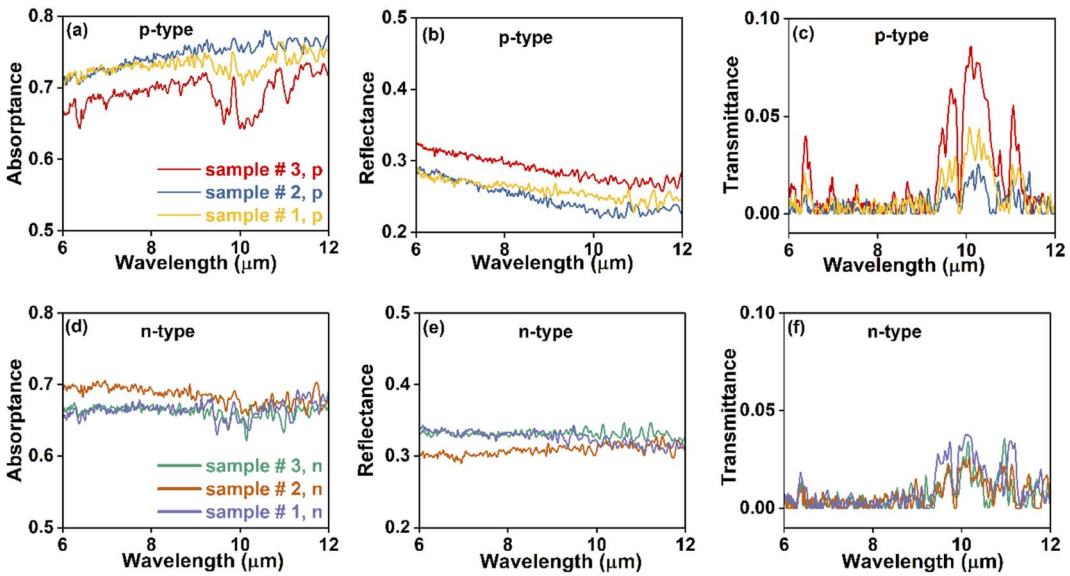

Fig. 3 FTIR spectrum measured by DRIFTS of printed (a–c) p and (d–f) n- type films with different thicknesses: sample #1, sample #2, and sample #3.

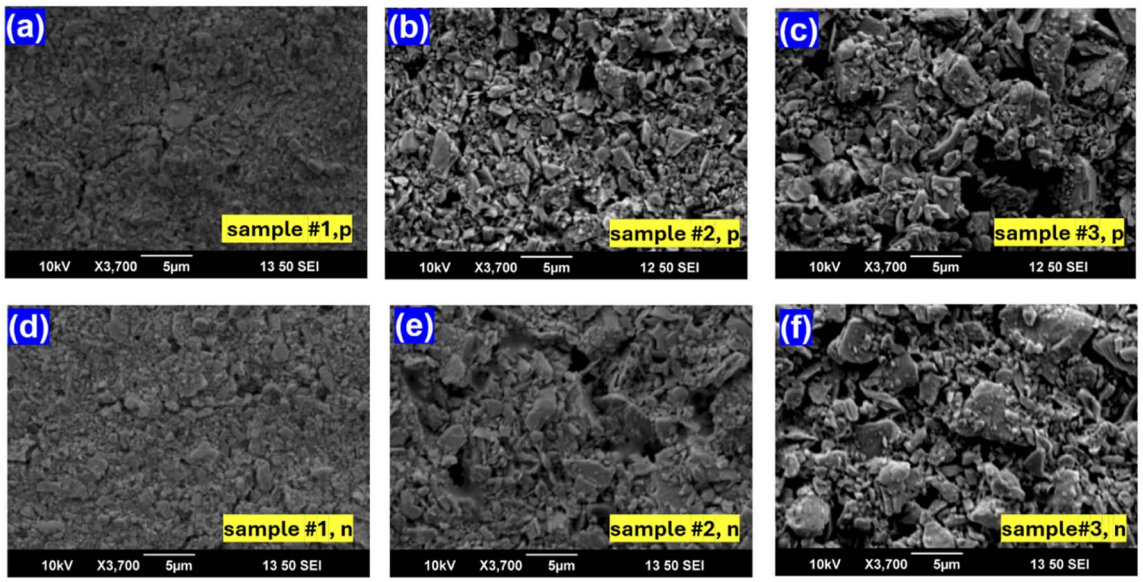

Fig. 4 SEM micrographs of the printed Sb–Bi–Te-based p- type film (a) sample #1, p, (b) sample #2, p, and (c) sample #3, and p and n-type (d) sample #1, n, (e) sample #2, n, and (f) sample #3, n.

tests, and the resulting data are plotted in Fig. 5. The graphs show the normalized resistance of the p-type and n-type films with bending cycles. Our data indicate that the films are stable and flexible, as no cracks or breaks were observed after the test. However, the normalized resistance slightly increases with the number of bending cycles. For p-type printed films, the normalized resistance increases up to 50% after 100 bending cycles. For smaller bending radii, the increase is slightly more pronounced. In contrast, in n-type devices the increase in normalized resistance is not substantial for all thicknesses and both bending diameters. This change may be because of several factors. First of all, as mentioned in Section 2.2 the p-type and n-type ink contains different concentrations of the binder (5% and 10% respectively). This has a major influence on the inter particle bonding of the thermoelectric particles. This can lead to a change in resistance and crack initiations. Thinner samples of both p- and n-type films exhibited better mechanical stability, suggesting reduced strain effects with lower thickness. The mechanical flexibility of the printed single legged and double legged film is depicted in Fig. S3(a and b).

3.3. Thermoelectric properties of printed p- and n-type TE films

TE performance of the printed films is crucial, which governs the films' PTE responsivity. Therefore, the electrical

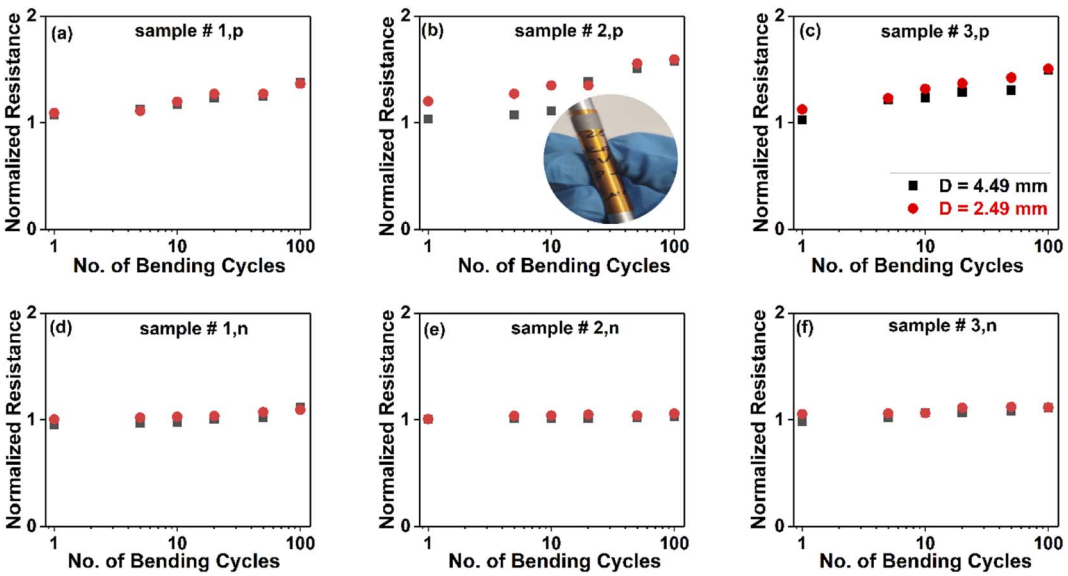

Fig. 5 Normalized resistance *vs.* number of bending cycles for (a–c) single p and (d–f) n-type devices with different samples with thicknesses t_1, t_2 and t_3.

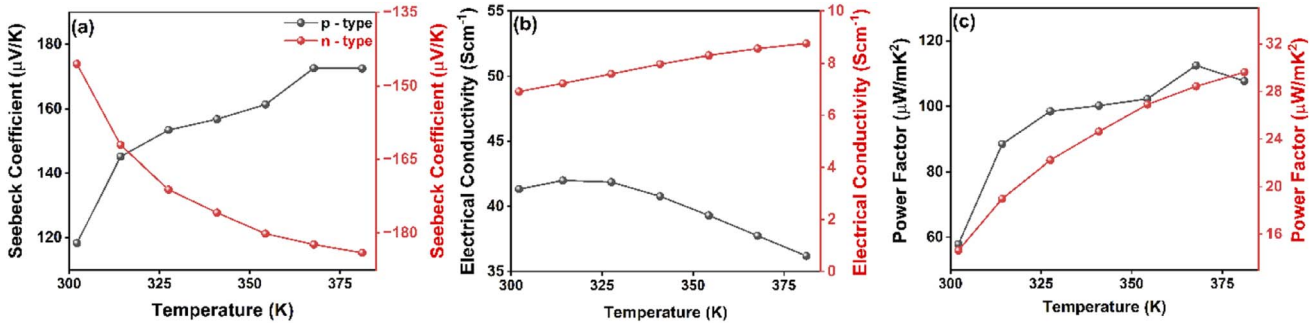

Fig. 6 Thermoelectric characterization: (a) change in the Seebeck coefficient α, (b) electrical conductivity σ, and (c) power factor with temperature for p and n -type materials.

conductivities (σ) and Seebeck coefficients (α) of printed p- and n-type films were measured from room temperature (RT) to 380 K (*cf.* Fig. 6). Since RT measurements showed negligible variation in α and σ values with varying thickness, time dependent TE performance was recorded for the intermediate printed films (sample #2, p and sample #2, n). For a p-type material, the α value is approximately 120 μV K^{-1} at RT, and for an n-type material, it is −143 μV K^{-1}. In the conductivity graph of the p-type printed film, we observe that the conductivity at RT is 41 Scm^{-1}, peaks at approximately 310 K, and then decreases steadily toward 400 K. This suggests that the carrier mobility decreases due to enhanced phonon scattering at higher temperatures. For the n-type printed film, the conductivity at RT is 7 Scm^{-1} and increases gradually from 300 K to 400 K, indicating an increase in charge-carrier mobility or carrier concentration with increasing temperature.

The conductivities of n and p-type differ mainly because of different carrier concentrations, carrier mobilities and microstructural pathways. The p-type printed films show higher electrical conductivity than n-type even after having a lower carrier concentration. This is because the p-type material has a significantly higher carrier mobility. The more detailed transport phenomena are discussed in our previous report.[29] However, the absolute value of transport parameters of the printed material, specifically conductivity, differ from the previous report due to different post printing process conditions. The power factor for the p-type and n-type printed films increases with increasing temperature, mainly due to the increasing absolute value of the Seebeck coefficient. The thickness variation of the printed films is in the range of 12 to 30 μm. These dimensions are much higher than the dimensions where variations in TE properties like the Seebeck coefficient and conductivity due to the size-dependent electronic effects occur. This is mainly controlled by the percolated phase of Bi–Sb–Te. The Seebeck coefficient and electrical conductivity of sample #1 and sample #2 at room temperature were measured and are given in Table S3.

3.4. Performance of the PTE infrared sensors

So far, the optical and TE properties of the individual printed p- and n-type legs have been discussed, which govern the performance of the PTE sensors. Now, a CO_2 laser maintained at 294 ± 1 K, which emits an infrared radiation of 10.6 μm, was used to evaluate the PTE performance of the individual p- and n-type single-legged and double-legged (a single thermocouple) PTE sensors. One side of the printed PTE infrared sensors was exposed to the CO_2 laser, where the incident radiation was converted into thermal energy *via* photothermal conversion, resulting in a temperature increase at the illuminated surface. The temperature gradient between the hot and cold sides of the sensors induces an electrical signal *via* the thermoelectric effect. The optical absorptance and geometrical properties of the TE legs govern the first conversion step (photothermal).

In contrast, the Seebeck coefficient of each leg determines the second step (thermoelectric conversion). The responsivity (R) of a PTE infrared sensor is defined as the ratio of the electric output signal to the absorbed incident radiation power.[15] Mathematically, it can be expressed as:

$$R_V = \frac{V}{P} \quad (2)$$

where V is the output voltage of the PTE sensor, and P is the incident radiation power.

Output voltage as a function of incident laser power for the printed single-legged n-type, p-type, and double-legged PTE infrared sensors is shown in Fig. 7(a–c). The voltage increases with increasing laser power. The responsivities of the sensors were estimated at room temperature by evaluating the ratio of the output voltage to the incident laser power. The total output voltage is nearly doubled for the double-legged PTE IR sensor [Fig. 7(c)] and yields a high responsivity of ∼107.7 mV W^{-1}. The thickness dependent S values are shown in Fig. 7(d–f). The improved voltage responsivity at lower thermal mass is evidenced by the higher responsivity with decreasing film thickness across all configurations even though the intermediate thickness t_2 exhibited higher absorptivity. This shows that photo-thermoelectric responsivity depends both on optical absorption and thermal conversion *via* the Seebeck effect. The film with thickness t_2 with a higher void area fraction absorbs more radiation compared to the thinnest film, but due to the significantly higher thermal mass, a lower temperature difference is induced (*cf.* Fig. S1 and Table S2). Although higher thermal mass facilitates a faster temperature increase, a lower

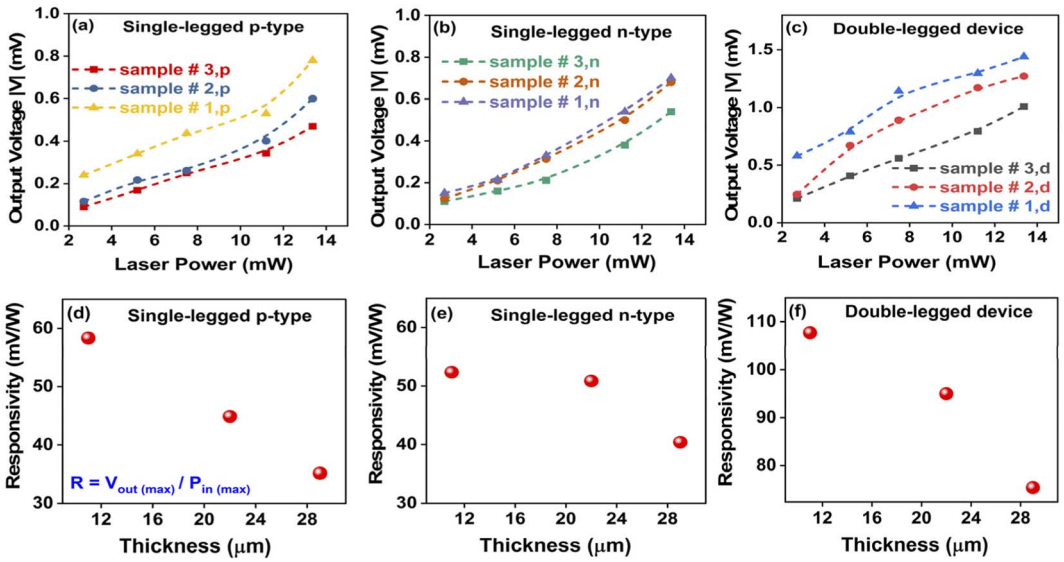

Fig. 7 Output voltage as a function of incident laser power for single-legged (a) p -type and (b) n-type devices, and (c) double-legged PTE devices with different thicknesses t_1, t_2 and t_3. Change in responsivity with thickness of (d) p-type, (e) n-type, and (f) double legged PTE devices.

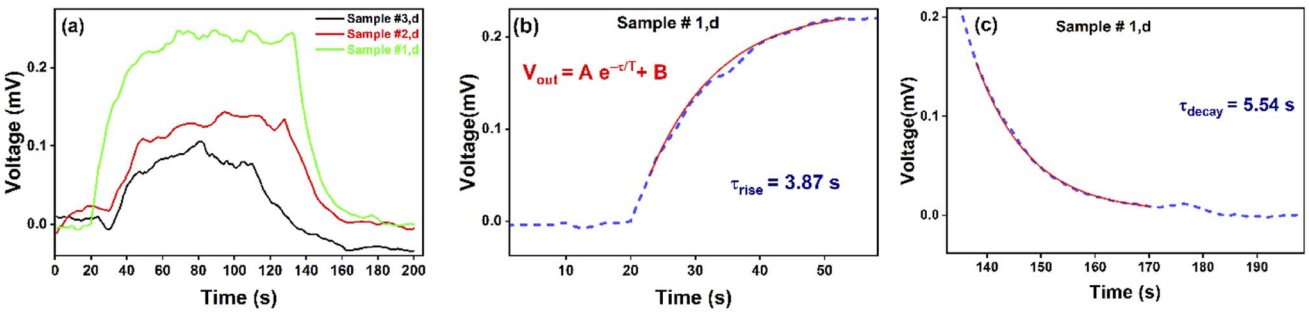

Fig. 8 Output voltage *vs.* time graph of (a) double-legged devices with different thicknesses, t_1, t_2 and t_3. (b and c) Calculation of response time by fitting the curve.

temperature gradient leads to lower Seebeck voltage, which overrides the small difference in optical absorption. The temporal response ($R(t)$) of PTE sensors can be defined as the ratio of the output voltage (V_{out}) to the maximum reachable voltage for a constant input power:

$$R(t) = \frac{V_{out}(t)}{V_{max}} \quad (3)$$

The temporal response of printed single-legged p and n type and double-legged devices has been studied by exposing them to laser radiation while maintaining the laser's ON and OFF states for 30 seconds each. The responses of double-legged devices with varying thicknesses are compared in Fig. 8(a). To have a detailed picture of the response curve of the double-legged device, the time dependent rise and decay of the output voltage $V_{out}(t)$ for each thickness t_1, t_2 and t_3 have been studied using the following equations:

$$V_{out} = Ae^{\frac{-\tau}{T}} + B \quad (4)$$

where τ is the time constant, and A and B are the fitting parameters[30] for the case of a rising or a decaying signal, respectively. The fitted graphs of double-sample #3 are shown in Fig. 8(b) and (c). The device with the smallest thickness t_1, exhibits a faster response than the other two devices according to the calculated response time (see Table S4 for a comparison). These results show that making the device thinner improves the signal due to the reduced thermal mass. The double-legged device architecture also improves voltage, which together leads to better photodetection performance. This study emphasizes the essential roles of device architecture and thickness in enhancing the responsivity and temporal response of printed PTEs for laser sensing applications.

4. Comparison with device simulations

The simulation study was conducted using COMSOL Multiphysics version 6.3, employing the finite element method, to evaluate the influence of the parameters on the tested device's

thermal and electrical behavior and to explore the underlying transport physics. The device dimensions were based on physical dimensions taken from fabricated devices. The thermoelectric material properties, including the Seebeck coefficient and electrical conductivity as functions of temperature, were derived from experimental measurements and subsequently implemented in the COMSOL Multiphysics framework to provide a more accurate representation of the device behavior. In the simulation, we mimicked the real device geometries including the impinging laser beam, and combined heat transfer in solids to determine the spatiotemporal temperature distribution caused by the laser source. The incident photons from the laser are absorbed at the surface of one side of the PTE device and converted into heat, thereby raising the temperature of the exposed area. This localized heating creates a temperature difference across the printed PTE devices with the opposite side remaining at a lower temperature. This thermal gradient drives charge carriers within the material, generating a Seebeck voltage. This simulation framework predicts temperature distribution and voltage generation. Table S7 summarizes the simulation parameters and material properties used in this study. The open-circuit voltage and average surface temperature responses to laser irradiation at different times during transient simulations for the double-legged PTE sensors are shown in Fig. 9. As seen in Fig. 9(a) and (b), incident laser photons are absorbed at the surface of the thermoelectric leg, quickly converting into heat and raising the temperature in the exposed area. The temperature distribution is shown for a time delay of 0.1 ms and after 50 seconds of irradiation.

This localized heating creates a temperature gradient across the n- and p-type legs, thereby driving carrier diffusion and generating a voltage, as illustrated in Fig. 9(d). This generates a thermal gradient that drives charge carriers within the material, producing a Seebeck voltage and electrical power when under load. The resulting thermoelectric response, shown in Fig. 10(c), demonstrates a Seebeck voltage of approximately

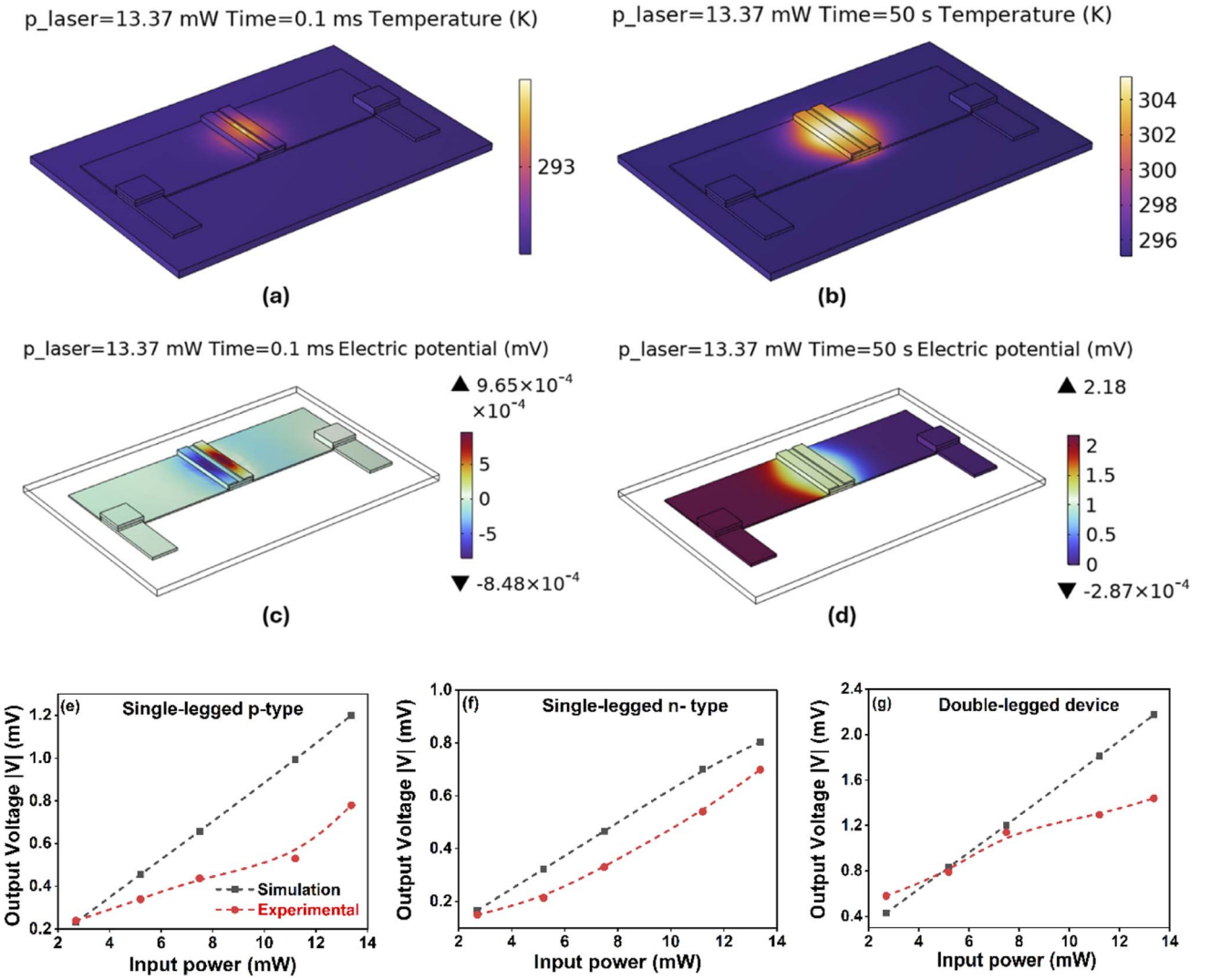

Fig. 9 COMSOL simulated model of Bi_2Te_3-based printed double legged (a) and (b) simulated temperature distributions of a double legged device. (c and d) Corresponding output voltages at different laser irradiation times and comparison between simulation and experimental output voltage for t_1 thick (e) single-legged p-type, (f) single-legged n-type, and (g) double-legged devices.

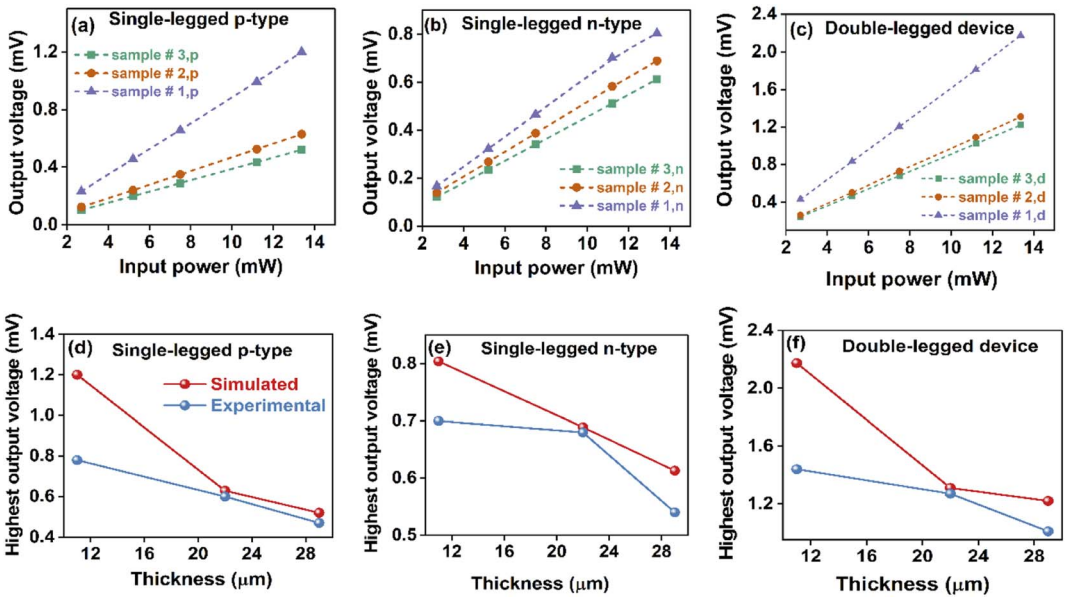

Fig. 10 Simulated input power *vs.* output voltage for single-legged (a) p-type, (b) n-type, and (c) double-legged devices, and comparison of simulated and experimental highest output voltage with thickness of single-legged (d) p-type, (e) n-type, and (f) double-legged devices.

2.17 mV, exceeding that of the single-leg design at the same thickness. This voltage enhancement arises from the cooperative contribution of the p- and n-type legs and is entirely consistent with experimental observations. Fig. S4 and 10(a) and (b) display the corresponding data for single-legged devices.

Fig. 9(e–g) shows a comparison between simulation and experimental output voltage for (e) single p-type, (f) single n-type, and (g) double legged devices with a thickness of 11 μm at different input powers. A comparison between the simulated and experimental output voltage at maximum input power was carried out and is shown in Fig. 10(d–f). The comparison between highest output voltage from the simulation and experiment shows that the experimental trend of an increase in output voltage with a decrease in thickness is reproduced in simulations also. There is a good agreement of the trend for the single-legged devices, whereas for double-legged devices, the thickness dependence is considerably stronger is the experiment than the simulation model. So together with the absorbed power normalization results in Fig. S2, we can conclude that the photo-thermoelectric behavior is a combined effect of optical absorption and thickness dependent thermal behavior.

5. Conclusion

Apart from application in solid-state cooling and energy harvesting, thermoelectric technology holds significant potential for radiation detection including infrared sensing *via* the photo-thermoelectric effect. Our work explored printing-enabled geometric tuning of Sb–Bi–Te-based n- and p-type TE films to achieve enhanced PTE responsivity for infrared sensing. The thickness dependent microstructural, optical, and TE properties were studied, revealing their collective impact on PTE performance. Single-legged and double-legged PTE infrared sensors with different thicknesses were fabricated using these printed TE materials. When exposed to 10.6 μm CO_2 laser irradiation, all sensors exhibited stable, reversible, and linear voltage responses proportional to the incident power. Thinner sensors demonstrated better densification, lower porosity, enhanced mechanical flexibility, and higher PTE responsivity. Furthermore, the double-legged PTE infrared sensors exhibited a higher output signal than single-leg designs, confirming the additive Seebeck effect from p- and n- type TE materials. The thinnest sensor, at 11 μm, achieved the highest responsivity of 107.7 mV W^{-1}. The superior performance can be attributed to its reduced thermal mass and efficient thermal-to-electrical conversion. Hence, thickness engineering offers a straightforward yet effective method to optimize printed PTE infrared sensors. Combined with scalable screen printing, mechanical flexibility, room-temperature operation, and adjustable performance, these sensors are promising for next-generation wearable electronics, human–machine interfaces, and distributed environmental monitoring systems.

Conflicts of interest

The authors declare no conflict of interest.

Data availability

The data supporting this article have been included as part of the supplementary information (SI). Supplementary information is available. See DOI: https://doi.org/10.1039/d6ta05248g.

Acknowledgements

The authors acknowledge funding by the European Research Council, grant 101097876 – ORTHOGONAL. The authors wish to acknowledge the Deutsche Forschungsgemeinschaft (DFG,

German Research Foundation) under Germany's Excellence Strategy *via* the Excellence Cluster 3D Matter Made to Order (EXC-2082/2). The German Federal Environmental Foundation (Deutsche Bundesstiftung Umwelt - DBU), through the DBU Ph.D. scholarship program, also supported this. We also acknowledge support from the Karlsruhe School of Optics & Photonics (KSOP).

References

1 K. Yazawa, J.-H. Bahk and A. Shakouri, *Thermoelectric Energy Conversion Devices and Systems*, WORLD SCIENTIFIC, 2021, vol. 07.
2 D. M. Rowe, *Thermoelectrics Handbook: Macro to Nano*, CRC press, 2005.
3 D. M. Rowe, *Renewable Energy*, 1999, **16**, 1251–1256.
4 N. Dhariwal, P. Yadav, Akanksha, S. Bisht, R. Chandra, O. P. Thakur, P. V. Braun, S. B. Kang, A. Sanger and V. Kumar, *Adv. Energy Mater.*, 2025, **15**, 2502895.
5 J. Zang, J. Chen, Z. Chen, Y. Li, J. Zhang, T. Song and B. Sun, *J. Mater. Chem. A*, 2021, **9**, 19439–19464.
6 A. W. Van Herwaarden and P. M. Sarro, *Sens. Actuators*, 1986, **10**, 321–346.
7 X. Lu, L. Sun, P. Jiang and X. Bao, *Adv. Mater.*, 2019, **31**, 1902044.
8 Y. Zou, Z. Zhang, J. Yan, L. Lin, G. Huang, Y. Tan, Z. You and P. Li, *Nat. Commun.*, 2022, **13**, 4372.
9 C. Chen, H.-L. Yu, Y.-M. Zhao, P.-X. Hou, S.-Y. Guo, S.-Q. Li, H.-Z. Wang, K. Tai and C. Liu, *Chem. Eng. J.*, 2024, **497**, 154263.
10 H. Zhou, P. Tao, Y. Lin, Z. Chen, Y. Zhao, W. Zeng, S. Wang, Z. Chen, G. Li and L. Ruan, *J. Mater. Chem. A*, 2021, **9**, 14958–14968.
11 J. Wang, Z. Xie, G. Lu, J. A. Liu and J. T. W. Yeow, *Microsyst. Nanoeng.*, 2023, **9**, 21.
12 J. Wang, Z. Xie, J. A. Liu and J. T. W. Yeow, *J. Mater. Chem. C*, 2022, **10**, 15105–15113.
13 G. Lu, J. Wang, W. Gao, Z. Xie, R. Zhou and J. T. W. Yeow, *IEEE Nanotechnol. Mag.*, 2025, **19**, 6–13.
14 D. Zhang, T. Feng, H. Hou, J. Yang, G. Liu, J. Liu and G. Qiao, *Mater. Sci. Semicond. Process.*, 2026, **201**, 110088.
15 S. Wredh, M. Dai, K. Hamada, M. A. Rahman, N. Q. Adanan, G. Zamiri, Q. Y. S. Wu, W. Zhai, N. W. L. Mun, Z. Dong, W. Kubo, Q. J. Wang, J. K. W. Yang and R. E. Simpson, *Adv. Opt. Mater.*, 2024, **12**, 2401450.
16 J. Liao, H. Shao, Y. Zhang, Y. Yan, J. Zeng, C. Lan, B. Gao, D. Chen, Q. Quan, P. Xie, Y. Meng and J. C. Ho, *Adv. Mater.*, 2025, **37**, 2419653.
17 D. Wang, S. Liu, L. Liang, C. Zhao, D. Liu, B. Zhang, J. Pan, X. Chen, X. Yang, H. Dang, D. Li, G. Liu, D. Wang, D. Fang, F. Liu, J. Cao, L. Li, Y. Zhang, D. Jiang, X. Fang, J. Sui, L. Zhao, Z. Niu and J. Zhu, *Room Temperature long-wavelength infrared Sensitive Imaging Photodetect ion based on topological insulator Bi_2Te_3 nanoflakes*, 2026, DOI: 10.21203/rs.3.rs-8659972/v1.
18 Y. Zhang, J. Jiang, Z. Zhang, H. Yu, Y. Lian, C. Han, X. Liu, J. Han, H. Zhou, X. Dong, J. Gou, Z. Wu and J. Wang, *J. Mater. Chem. C*, 2024, **12**, 16714–16721.
19 J. Jiang, X. Fan, H. Yu, Y. Lian, J. Xie, L. Liu, B. An, Y. Yan, J. Han, W. Li, J. Gou, Z. Wu and J. Wang, *Adv. Opt. Mater.*, 2025, **13**, e02244.
20 C. Chen, H.-L. Yu, Y.-M. Zhao, P.-X. Hou, S.-Y. Guo, S.-Q. Li, H.-Z. Wang, K. Tai and C. Liu, *Chem. Eng. J.*, 2024, **497**, 154263.
21 E. Moisello, M. E. Castagna, A. La Malfa, G. Bruno, P. Malcovati and E. Bonizzoni, *Micromachines*, 2022, **13**, 934.
22 C. Guo, J. Jiang, H. Hou, J. Yang, D. Zhang, Q. Lv, J. Liu and G. Qiao, *Sens. Actuators, A*, 2026, **399**, 117448.
23 J. Wang, Z. Xie, G. Lu, J. A. Liu and J. T. W. Yeow, *Microsyst. Nanoeng.*, 2023, **9**, 21.
24 H. Fang, X. Xie, K. Jing, S. Liu, A. Chen, D. Wu, L. Zhang and H. Tian, *Nano-Micro Lett.*, 2025, **17**, 229.
25 Y. Li, F. Zhang, S. Wang, D. Li, Y. Sun, Z. Gao, Z. Wu and D. Zheng, *Nano Res.*, 2026, **19**(2), 94908400.
26 Y. Zheng, H. Xie, Q. Zhang, A. Suwardi, X. Cheng, Y. Zhang, W. Shu, X. Wan, Z. Yang, Z. Liu and X. Tang, *ACS Appl. Mater. Interfaces*, 2020, **12**, 36186–36195.
27 B. Zhu, X. Su, S. Shu, Y. Luo, X. Y. Tan, J. Sun, D. Sun, H. Zhang, Q. Zhang, A. Suwardi and Y. Zheng, *ACS Appl. Energy Mater.*, 2022, **5**, 2002–2010.
28 A. Sarbajna, A. G. Rösch, L. Franke, U. Lemmer and M. M. Mallick, *Adv. Eng. Mater.*, 2023, **25**, 2200980.
29 M. M. Mallick, L. Franke, A. G. Rösch, H. Geßwein, Z. Long, Y. M. Eggeler and U. Lemmer, *Adv. Sci.*, 2022, **9**, 2202411.
30 M. M. Mallick, L. Franke, A. G. Rösch, M. Hussein, Z. Long, Y. M. Eggeler and U. Lemmer, *Adv. Funct. Mater.*, 2024, **34**, 2301681.

